THE JOURNAL OF PHYSICAL CHEMISTRY C
A JOURNAL OF THE AMERICAN CHEMICAL SOCIETY

pubs.acs.org/JPCC Article

Anion Effects on the Interfacial Structure and Bulk Physical Properties in Choline-Based Hydrogen-Bonded Electrolytes

William Dean, Drace Penley, Yun-Yang Lee, Raziyeh Ghahremani, Saudagar Dongare, and Burcu Gurkan*

Cite This: https://doi.org/10.1021/acs.jpcc.2c01901 Read Online

ACCESS | Metrics & More | Article Recommendations | Supporting Information

ABSTRACT: Electrolytes consisting of choline (Ch) salts with acetate (Ac) and oxalate (Ox) anions were studied in mixtures with ethylene glycol (EG), in comparison to chloride (Cl)- and bis(trifluorosulfonyl)imide (TFSI)-containing systems to understand the impact of anion size and charge density on the bulk electrolyte and interfacial properties. These represent hydrogen-bonded concentrated electrolytes where the Ch salts are the H-bond acceptors (HBAs) and EG is the H-bond donor (HBD) in 1:2 and 1:4 HBA:HBD ratios. Increased H-bonding in Ch_2Ox with EG compacts the liquid compared to ChAc, consistent with the increased dissociation energies of the HBA:HBD clusters with Ox^{-2} calculated by density functional theory (DFT), thus leading to denser and more viscous liquids. Electrochemical impedance spectroscopy (EIS) and surface-enhanced Raman spectroscopy (SERS) were used to investigate interfacial charge density and the electrode surface species. Differential capacitance curves demonstrate weak dependence on potential except for ChAc:EG, where Ac^- is found to adsorb on the Au surface, in particular at +0.055 V vs Ag quasi-reference while no specific adsorption was observed on glassy carbon (GC). In situ SERS measurement confirms the formation of a surface layer in the ChAc:EG systems resulting from a Au−acetate interaction. Despite the structural similarities, Ox^{-2} did not show specific binding or any dependence of capacitance on potential as a result of strongly solvating EG molecules via H-bonds. This study shows that the charge density of the HBAs impacts both bulk properties and the electrical double-layer formation in concentrated H-bonded electrolytes that is relevant to electrochemical kinetics and morphology in electrodeposition processes and energy storage applications.

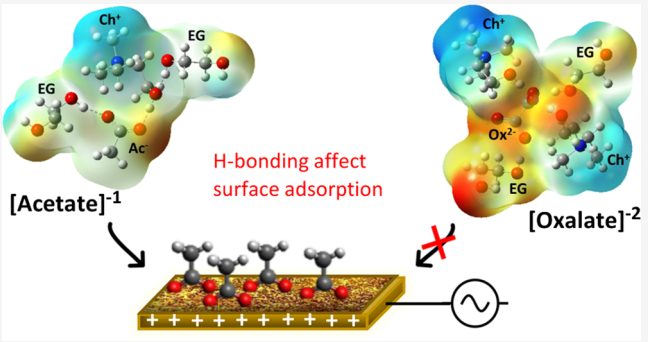

INTRODUCTION

Concentrated electrolytes such as ionic liquids (ILs) and deep eutectic solvents (DESs) possess wide electrochemical windows, high solvent strengths, and low volatilities, which make them promising electrolytes for electrochemical applications such as electrodeposition[1−3] and energy storage devices.[4−9] DESs have gained increased attention over the past two decades due to their lower costs than ILs and easier synthesis. DESs are commonly composed of salts such as choline chloride (ChCl) that act as hydrogen-bond acceptor (HBA) and neutral molecules such as ethylene glycol (EG) that act as hydrogen-bond donor (HBD).[10] Certain HBA and HBD mixtures at a specific composition yield liquids that have significantly depressed freezing points compared to the parent compounds.[11] DESs commonly studied in electrochemical applications contain high concentrations of Cl^-, and in our previous study, we reported specific adsorption of Cl^- on metal electrodes.[12] There have been no comprehensive interfacial studies on DESs or more broadly the eutectic solvents with H-bonding based on organic anions or anions with charges other than −1. This study presents Cl-free organic eutectic solvents with varying anion structure and charge density to understand the influence of the anion on bulk and interfacial electrolyte properties.

The liquid structure of DESs is governed by a complex hydrogen-bonding network as well as Coulombic interactions due to the high salt content.[13,14] Experimental and computational studies have shown that the formation of the H-bonding network within DESs has a large impact on their physical properties, liquid structure,[14] solvation dynamics,[15] and charge transfer phenomena in electrochemical systems.[16] The physical properties of eutectic solvents have been shown to be highly dependent on their components,[17−19] molar composition,[20,21] and water contents.[15,22,23] DESs typically have high viscosities and high salt concentrations[24,25] and researchers continue to

Received: March 18, 2022
Revised: July 31, 2022

https://doi.org/10.1021/acs.jpcc.2c01901
J. Phys. Chem. C XXXX, XXX, XXX−XXX

look for DES systems with low viscosity, as it contributes to low transport resistance for charge carriers within the electrolyte.[26,27] Ethaline, a mixture of ChCl and EG at a 1:2 molar ratio, has been the subject of many studies due to its relatively low viscosity (36−52 cP).[24] Klein et al.[21] studied changes in the physical properties of the hydrogen-bonded electrolyte with compositional changes of ChCl and EG. Interestingly, the 1:4 ChCl:EG mixture was the most ionically conductive despite its higher viscosity compared to 1:2 and 1:6 mixtures, highlighting the importance of microscopic environments in DESs and H-bonded solvents. It has been shown that hole theory, a mechanism of transport where ions move through holes in the solvent structures in ILs, is also applicable to changes in viscosity and conductivity in DESs.[17,21] Tuning DES components to lower the viscosity while maintaining the beneficial aspects they have to offer is critical for practical applications of these electrolytes for energy storage.[24,25]

A recent study by Spittle et al.[28] showed that the addition of ChCl salt to the H-bonding network of glycerol (Gly) and EG induces microscopic structural heterogeneities in the liquid that correlate with bulk properties. They report that in HBDs with a strong H-bonding network such as Gly, the Ch^+ cation is caged in the network while the Cl^- anion weakens the self-interactions of Gly−Gly. This study motivated us to examine the impact of anion size and charge density in these DESs and similar mixtures where H-bonding plays an important role in determining the physical properties.

While the transport properties such as viscosity and conductivity of an electrolyte are directly related to performance in electrochemical processes, interfacial properties such as the double-layer structure and electrode surface species are also important as they relate to the mechanism and kinetics of electron transfer reactions. Species complexation[29] and solvation[21] affect electron transfer reactions; therefore, kinetic studies by classical electroanalytical techniques require caution and understanding of the structure and interfacial species.[16,27,29,30] To develop concentrated DES-like electrolytes with high energy density, it is critical to understand not only the bulk liquid properties but also the interfacial properties. Specifically, the liquid structure near the electrode surface and the surface species that play a role in electron transfer are not generally as well understood in these systems.

Most studies thus far have focused on ChCl-based DESs, and they indicate that some degree of ordered structure forms with surface adsorption playing a dominant role in the electrode-DES interface. Vieira et al.[31] used polarization modulation infrared reflection absorption spectroscopy (PM-IRRAS) to study ethaline on a glassy carbon electrode. They observed surface adsorption of Ch^+ at negative potentials and saw evidence of reorientation of Ch^+ with increased negative polarization to allow closer packing. Chen et al.[32] performed potential-dependent atomic force microscopy (AFM) measurements on a highly ordered graphite electrode, showing a structured inner layer that was cation-rich at negative potentials and changed to anion-rich at positive potentials. Figueiredo et al.[33] used electrochemical impedance spectroscopy (EIS) to show that the DES glyceline (ChCl:Gly, 1:2 molar ratio) behaves very differently on different electrode surfaces. In our previous study, we investigated the potential-dependent capacitance for several ChCl:EG systems at glassy carbon (GC), Au, and Pt electrode surfaces using the EIS technique.[12] Shallow U-shaped capacitance was observed for the systems on GC; interestingly, this is similar to what has been seen for dilute electrolytes. Using a modified Gouy−Chapman model, the interface on a GC electrode was modeled as a diffuse layer of charge extending to the bulk electrolyte.[34,35] Au and Pt showed much more complex differential capacitance behavior, attributed to the surface adsorption of Cl^-. Wu et al.[36] observed similar behavior in capacitance curves for ethaline and confirmed Cl^- adsorption using shell-isolated nanoparticle enhanced Raman spectroscopy (SHINERS). Additionally, they investigated a ChCl-based DES with lactic acid as the HBD, and they found evidence of HBA adsorption, but that surface adsorption of the Cl^- anion still dominated capacitive behavior.[37]

Computational studies of ChCl-based DES have also supported the formation of surface-normal nanostructures at the electrode−electrolyte interface in H-bonded electrolytes and DESs. Atilhan et al.[38] simulated mixtures of ChCl-levulinic acid on uncharged electrode surfaces using classical molecular dynamics, finding that both ions and solvent molecules form a strongly adsorbed layer on the electrode surface. Mamme et al.[39] observed the formation of an adsorbed layer of urea molecules and counterions in a mixture of ChCl:urea (1:2 molar ratio) under both positive and negative polarization, and the absorbed layer was followed by a mixed structured layer of Ch^+, Cl^-, and urea. Studies thus far have provided some insight into common phenomena that can occur at electrochemical interfaces in DESs, but most of these studies have been limited to ChCl-based systems, and thus knowledge outside of these systems is limited.

Adsorbed species at the electrode surface have been shown to have a large effect on the morphology in electrodeposition. Additives are frequently used to improve electrodeposition in aqueous mixtures by adsorbing to the electrode surface and occupying nucleation sites but are only recently investigated for DESs. In the DES ethaline, it has been suggested that strongly adsorbed Cl^- causes 2D deposited structures to form perpendicular to the surface during zinc deposition.[2] Small-molecule additives such as boronic acid and nicotinic acid have been used to improve uniformity by adsorbing to the electrode surface and displacing surface-adsorbed Cl^-.[2,40] Substituting the Cl^- with other anions in these Ch-based mixtures could eliminate the need for additives to achieve smooth depositions.

In this study, we investigated the impact of the anion on electrolyte properties and interfacial structure of concentrated H-bonded electrolytes consisting of HBAs of choline acetate (ChAc), choline oxalate (Ch_2Ox), and choline bis-(trifluoromethylsulfonyl)imide (ChTFSI) in EG with 1:2 and 1:4 molar ratios (structures shown in Table 1), similar to the DES, ethaline. As the anions are of different sizes and charges, we anticipate that the strength of the H-bonding network and the liquid structure would be effectively altered. Infrared spectroscopy and NMR spectroscopy were used to probe the changes in hydrogen bonding and the temperature-dependent densities, viscosities, and conductivities are reported as descriptors for changes in the microenvironment of the liquid. The surface tension of these samples was also measured to estimate the size of entropic voids according to the hole theory that is often applied for DESs and ILs to probe fluidity and species transport.[17,21] As both transport and interfacial properties are influenced by the solvation environment, we performed geometry optimization and calculation of energetics for possible anion solvation by EG and/or complexation with Ch^+ cation using density functional theory (DFT). EIS was used to determine potential-dependent differential capacitance

https://doi.org/10.1021/acs.jpcc.2c01901
J. Phys. Chem. C XXXX, XXX, XXX−XXX

Table 1. Structures of HBAs Investigated[a]

Chemical Structure	HBA	Water content (ppm)
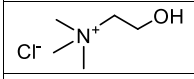	ChCl	460–550[12]
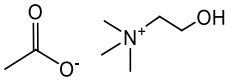	ChAc	550-730
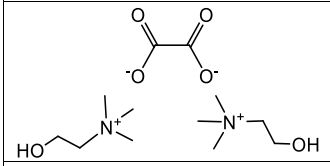	Ch_2Ox	230-410
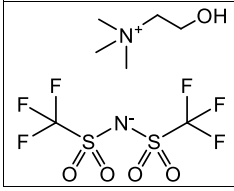	ChTFSI	290-320

[a]The water contents are for the HBA:HBD (1:2 and 1:4) mixtures. EG was used as the HBD.

for these mixtures, which can be related to the general interfacial charge density. Potential-dependent changes in the inner surface layer of ions at the interface were studied on the Au surface by surface-enhanced Raman spectroscopy (SERS). SERS is highly sensitive and is commonly employed to study changes of species in proximity (<10 nm) to the electrode surface including surface adsorption,[41−44] molecular reorientations of ions,[45] and solute−solvent interactions.[21] Combining the EIS and SERS techniques allows for a more complete understanding of interfacial structure. It was found that surface adsorption is still present in some of the systems with organic anions and can play a dominant role in interfacial behavior. This is highlighted in the differences observed in capacitance curves and spectroscopically between the ChAc systems where adsorption is dominant and ChTFSI where anion adsorption is not seen. It was also found that the strong H-bonding interactions in the Ch_2Ox:EG can inhibit changes in interfacial charge density. This report contributes to the fundamental understanding of the impact of HBAs on both bulk properties and electrical double layer in DESs and concentrated H-bonded electrolytes as they relate to electrochemical applications.

MATERIALS

Choline chloride, ChCl (99%), and anhydrous ethylene glycol, EG (99.8%), were purchased from Acros Organics. Choline acetate, ChAc (98%), and choline bis(trifluoromethylsulfonyl)-imde, ChTFSI (99%), were obtained from Iolitec. Choline oxalate (Ch_2Ox) was synthesized using an acid−base reaction between choline hydroxide (Sigma-Aldrich, 46 wt % in water) and oxalic acid. Oxalic acid was dissolved in a minimal amount of methanol and was added dropwise to the choline hydroxide solution in a 200 mL round-bottom flask. The solution was stirred and heated at 60 °C for 24 h. Residual solvent was evaporated off using a rotary evaporator at 60 °C. The resultant yellow solid was dried under vacuum for 24 h at 70 °C. For confirmation of synthesis, the sample was analyzed by NMR (see ^{1}H NMR and ^{13}C NMR, Figures S1 and S2, respectively). Elemental analysis of Ch_2Ox was performed by combustion ion chromatography (Atlantic Labs) to determine halide content. Halide impurity was determined to be below the detection limit of combustion ion chromatography (<0.25%). Nitrogen gas (99.998%) was received from Airgas. Gold quartz QM crystals (0.25 mm thick, 99.998%) were purchased from Fil-tech. Silver wire (1 mm in dia. 99.999%) was purchased from Alfa Aesar. The deuterated solvent DMSO-d_6 (10 mL, 99.9%) was purchased from Cambridge Isotope Laboratories, Inc. NMR tubes (5 mm OD; 7″ L; wall thickness: 0.38 mm) with coded closed caps were purchased from Bruker.

To prepare the electrolytes, ChAc, Ch_2Ox, and ChTFSI were dried under vacuum at 80 °C for 24 h. EG was dried using molecular sieves prior to use (water content ∼ 100 ppm). The water contents of the mixtures were determined using Karl−Fisher titration and are included in Table 1. All mixtures were prepared by mixing the components under a dry argon environment (VTI glovebox, H_2O < 1 ppm, O_2 < 1 ppm) at 80 °C for 1 h. Samples were then allowed to cool to room temperature and further deaerated by bubbling dry nitrogen before any of the measurements.

PHYSICAL PROPERTY MEASUREMENTS

A Rheosense viscometer was used to measure the viscosity of the samples; an enclosed temperature controller (viscosity ± 2% and temperature ± 0.1 K) was used to adjust the temperature of the sample in 5 °C increments. Conductivity measurements were taken using a dual platinum electrode cell (MMA 500 from Biologic INC) inside the RheoSense temperature control unit (±0.1 K). The samples were equilibrated at each temperature for 15 min prior to measurement. Density measurements were taken by an Anton Paar density meter (DMA 4500 M, accuracy of ±0.03 K and ±0.00005 g/cm^3) using temperature steps of 5 °C. Density, viscosity, and conductivity measurements were replicated three times at a given temperature for each system, and the average is reported.

Surface tension measurements were determined using a Kruss shape drop analyzer. The pendant drop method was used to determine the bulk surface tension of each mixture. A 1 mL syringe with a 1.8 mm diameter blunt-tip needle was used to ensure a large drop size. The surface tension can be related to the hole size (hole theory of diffusion) in each fluid, which is associated with the mobility of ions in concentrated liquid systems.[21] The average radius of holes in concentrated electrolytes is determined from the measured surface tension (γ) using eq 1.[46]

$$4\pi(r)^2 = 3.5\frac{k_B T}{\gamma} \quad (1)$$

where r is the average hole size, k_B is the Boltzmann constant, and T is the absolute temperature.

CHARACTERIZATION OF HYDROGEN BONDING

Fourier Transform Infrared Spectroscopy. A Thermo Scientific Nicolet iS50 FTIR was used to perform Fourier transform infrared (FTIR) spectroscopy measurements on the bulk electrolyte solutions to probe the changes in the H-bonding with HBA:HBD composition of the samples. All of the measurements were performed at room temperature (about 22 °C). Spectra were collected at 0.5 cm^{-1} resolution by taking an average of 32 scans.

https://doi.org/10.1021/acs.jpcc.2c01901
J. Phys. Chem. C XXXX, XXX, XXX−XXX

Proton and Pulse-Field Gradient Nuclear Magnetic Resonance Spectroscopy. ^{1}H NMR data were measured on a 500 MHz Bruker Ascend HD NMR to measure the extent of spectral shifts due to H-bonding. The sample temperature was controlled by the inner heating−cooling units to be 22 °C. The NMR samples for normal ^{1}H NMR were prepared by mixing 0.2 mg of samples in 0.6 mL of DMSO-d_6, and then loaded into the NMR tube. For the study of chemical shifts with different salt-HBD compositions, a coaxial tube set was used to prevent the mixing of salt-HBDs with the secondary solvent (DMSO-d_6), which may change the solvation environment. This procedure also eliminates the possibility of salt precipitation in dimethyl sulfoxide (DMSO). About 0.4 mL of the sample was loaded into the outer cell within the Ar atmosphere. An inner cell with DMSO/DMSO-d_6 (5/95 v/v) was then inserted into the outer cell containing the sample. The use of DMSO-d_6 is necessary for NMR frequency signal locking, and the addition of 5% DMSO (2.58 ppm) acts as the inner reference for the chemical shifts.

■ COMPUTATIONAL METHODS

Structure and Frequencies. Quantum mechanics calculations were carried out in the Gaussian16 program[47] using the three-parameter Becke model with the Lee−Yang−Par modification (B3LYP)[48] functional for exchange and correlation and the 6−311G++(d,p)[49] basis set. Structures of the isolated components and HBA:HBD mixtures and the associated electronic energies were obtained using geometry optimizations with default convergence criteria. To represent the concentrations used in the experimental studies for ChCl:EG, ChTFSI, ChAc:EG, and Ch_2Ox:EG, the number of EG molecules was increased from 1 to 4 while maintaining one Ch^+−$anion^-$ pair. Frequency calculations were carried out at the same level of theory to obtain Raman spectroscopic data. Raman frequencies were scaled by a factor of 0.964[50] for the ChTFSI system to compare with experimentally obtained spectra. Frequencies were not scaled for the ChAc system in accordance with the literature.[51]

Differential and Integral Analysis of Solvation. Two methods were used to determine the energy difference associated with adding a new EG to the solvent systems, following a similar methodology described by Penley et al.[52] The integral binding energy refers to the energy needed to add n EGs to a salt pair, e.g., ChAc + 2 EG → ChAc:EG (1:2). The more positive integral binding energy leads to a more thermodynamically stable system. In contrast, the differential binding energy is the energy to add one EG at a time, e.g., ChAc:EG (1:1) + EG → ChAc:EG (1:2). A positive differential binding energy indicates that it is thermodynamically favored for another EG molecule to be added to the H-bond network. The differential binding energy is useful for assessing the feasibility of different coordination structures with EG, whereas the integral binding energy is useful for assessing the relative stability of the H-bonding network.

■ ELECTROCHEMICAL MEASUREMENTS

Electrochemical measurements were performed in a dry positive-pressure nitrogen glovebox (Terra Universal) at room temperature (22 °C) using a Biologic SP−200 potentiostat. Working electrodes of glassy carbon (GC disk; 2 m dia) and gold (Au disk; 1.6 mm dia) were used for all electrochemical measurements. Electrodes were polished for 2 min with microdisks coated in 5 μm alumina for GC, and for Au, 3 μm diamond, followed by 5 μm alumina. Electrodes were rinsed with deionized water immediately following polishing. Measurements were iR-corrected using the resistance determined from a single-frequency (2500 Hz) impedance measurement. Cyclic voltammetry (CV) starting at open-circuit potential (OCP) at a scan rate of 20 mV/s (5 cycles) was employed to determine electrochemical windows; potentials are reported using a cutoff current density of 0.02 mA/cm^2. A T-cell configuration was used consisting of the working electrode, Pt wire counter electrode (1 mm dia), and Ag quasi-reference electrode (1 mm dia). EIS was used to determine the differential capacitance. A three-electrode setup was used with a 5 mL sample volume consisting of working electrode, carbon felt (2.5 cm^2) counter electrode, and Ag quasi-reference electrode (1 mm dia). EIS measurements were performed using a frequency range of 500 kHz to 100 mHz with an amplitude of 20 mV. EIS was taken at equally spaced potentials starting from OCP and moving to increasingly negative potentials. The potential was then returned to OCP using chronoamperometry for 30 min before starting a second sweep of EIS scans at positive potentials, similar to the procedure used by Klein et al.[53] to determine differential capacitance in ILs.

Differential Capacitance. The measured impedance encompasses all capacitive and resistive processes in the system. To identify the frequency range associated with the charging/discharging of the double layer, the complex capacitance plane, C (imaginary C'' versus real C' capacitance), as defined in eq 2 was examined, similar to previous studies for ionic liquids[53,54] and DESs.[12]

$$C = C' + iC'' = \frac{1}{i\omega Z} = -\frac{iZ'}{\omega(Z'^2 + Z''^2)} - \frac{Z''}{\omega(Z'^2 + Z''^2)} \quad (2)$$

where Z' and Z'' are the real and imaginary components of impedance, respectively. In the complex capacitance representation, a clear shoulder is observed, which corresponds to the formation of the electrical double layer, fitting this range to an equivalent circuit of a resistor in series with a constant phase element excludes slow processes captured at low frequencies. Differential capacitance was calculated using the fit parameters in eq 3.

$$C = \text{Average}\left[\frac{Q\omega_i^{a-1}}{\sin\left(\frac{a\pi}{2}\right)}\right] \quad (3)$$

where Q and a are fit parameters and ω_i is the angular frequency (Hz). In the case of U-shaped capacitance, a modified Gouy−Chapman equation (eq 4) was used to model capacitance in DESs as a diffuse layer of charge.[12]

$$C_{GC} = C_d \times \cos h\left(\frac{\alpha u}{2}\right) \quad \text{(Modified Gouy − Chapman)} \quad (4)$$

where C_{GC} is the Gouy−Chapman[36] capacitance, C_d is the Debye capacitance ($C_d = \frac{\varepsilon^*}{4\pi\lambda_D}$, where ε^* is the effective dielectric constant for the medium and λ_D is the Debye length), α is the ion interaction term, and u is the

https://doi.org/10.1021/acs.jpcc.2c01901
J. Phys. Chem. C XXXX, XXX, XXX−XXX

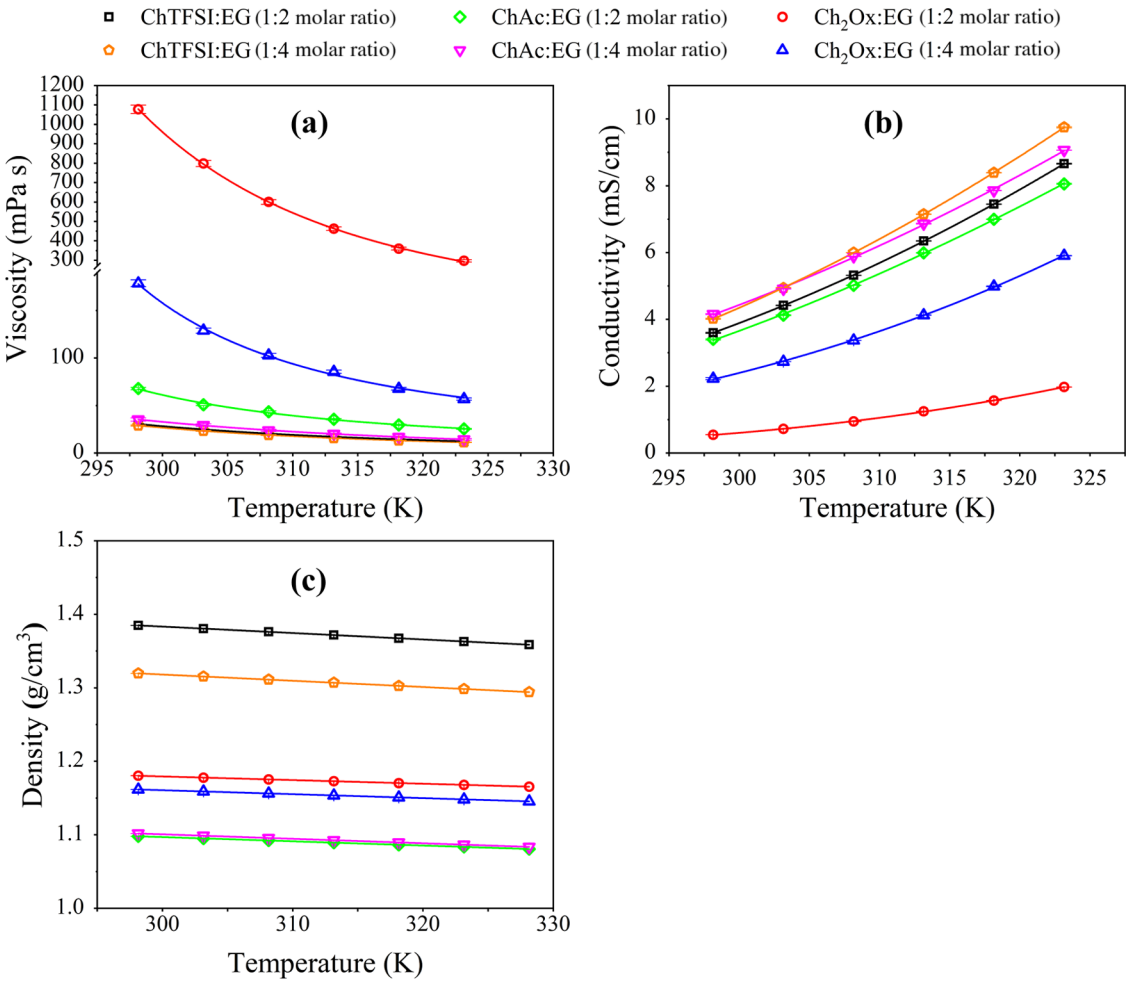

Figure 1. Temperature dependency of (a) viscosity, (b) conductivity, and (c) density of the Ch Anion:EG solvents at both 1:2 and 1:4 molar ratios. Viscosity and conductivity data were fit using Vogel−Fulcher−Tammann (VFT) theory (tabulated data are included in Table S1, and fit parameters are listed in Table S2).

dimensionless potential ($u = e\phi/k_bT$, where ϕ is the electrode potential with respect to the reference).

Constant Potential Electrolysis (CPE). To probe possible degradation of ChAc:EG (1:2) electrolyte close to the anodic/cathodic limits and confirm the electrolyte stability during EIS and SERS measurements, CPE was also performed. Experiments were conducted in a single-compartment cell with a three-electrode configuration. An Au surface (geometric surface area of 0.38 cm^2) was used as the working electrode with a Pt mesh as the counter electrode and Ag quasi-reference electrode (1 mm diameter). Potentials within the electrochemical window and close to the anodic and cathodic limits, as determined from CV, were applied for 2400 s. The headspace of the compartment was continuously purged during CPE with inert carrier gas (He) at a rate of 10 mL/min, to transport volatile reaction products from the cell to the online gas chromatograph, GC (7890B, Agilent Technologies). The GC is equipped with two thermal conductivity detectors (TCDs) for detecting CO and H_2, and one flame ionization detector (FID) for detecting hydrocarbons. The GC was calibrated using a standard gas mixture consisting of CO, CO_2, CH_4, C_2H_4, and C_2H_6 (0.0999 mol % for each component) balanced by He (Airgas, an Air Liquide Company) under standard conditions (1 atm, 298 K) to quantify gaseous degradation products. Automatic injections were performed at 20 and 40 min during the CPE experiment. Following CPE, the electrolyte was collected for analysis by ^1H and ^{13}C NMR to examine degradation products in the liquid phase.

POTENTIAL-DEPENDENT SURFACE-ENHANCED RAMAN SPECTROSCOPY (SERS)

An electrochemical cell, adapted from Klein et al.,[45] with an Au QCM crystal as the working electrode (0.2 cm^2), a coiled silver wire counter electrode, and a silver wire quasi-reference electrode (1 mm dia.) was used to collect Raman spectra under applied potential. The Au crystal was electrochemically roughened with a 0.1 M KCl solution using 24 cycles of a voltammetric sequence: starting with a chronoamperometry (CA) at −0.3 V (vs Ag quasi-reference) for 30 s, followed by linear sweep voltammetry (LSV) from −0.3 to 1.2 V, then a CA at 1.2 V for 1.2 s and an LSV from 1.2 to −0.3 V, a final CA returned to −0.3 V for 30 s.[55,56] The spectra were collected using a Horiba Xplora One Raman system with a 785 nm excitation laser at a spectral range of 600−2300 cm^{-1} (1 cm^{-1} resolution) with a 20× magnification objective, 500 mm hole, 200 nm slit, 10 s exposure time, and five accumulations. Localized Raman spectra were also obtained for smaller ranges of wavenumbers for spectral regions where significant potential-dependant change was observed to gain increased resolution (0.7 cm^{-1} resolution). SERS measurements were

https://doi.org/10.1021/acs.jpcc.2c01901
J. Phys. Chem. C XXXX, XXX, XXX−XXX

taken in the same potential range used for EIS measurements. Potential steps were taken across the electrochemical window of each mixture starting at OCP and stepping first to more positive potentials, then returning to OCP before the second step to negative potentials. Each potential was held for 5 min before taking the spectrum. Spectra were baseline-corrected using linear line subtraction.

RESULTS AND DISCUSSION

The temperature-dependent viscosities, conductivities, and densities of each solvent are shown in Figure 1. The Ch_2Ox:EG solvent (both 1:2 and 1:4 molar ratios) shows significantly higher viscosity and lower conductivity compared to ChTFSI:EG and ChAc:EG. For example, the viscosity of 1:2 Ch_2Ox:EG was found to be 1070 cP compared to 68 cP for 1:2 ChAc:EG and 30 cP for 1:2 ChTFSI:EG at 25 °C. Despite the similar structures of Ch_2Ox and ChAc, the increased charge density of Ox^{-2} and the divalent nature compared to Ac^- as well as the greater number of H-bonds that Ch_2Ox can form with EG lead to stronger intermolecular interactions. The stronger H-bonding network of Ch_2Ox:EG solvate is further justified by DFT calculations.

As seen in Table 2, the calculated integral binding energy of the Ch_2Ox:EG (13.26 eV) is higher than ChAc:EG (5.83 eV), thus suggesting a more rigid H-bonding network of Ch_2Ox:EG since the increase in integral binding energy indicates increased thermodynamic stability. The structural representations of all of the salt:EG clusters and the calculated charge densities are shown in Figure 2. Differential binding energies (Table S3) were positive for all systems, indicating that each addition of EG was thermodynamically favorable. The average H-bond length in Ch_2Ox:EG solvate cluster was 1.60 Å, while it was 1.80 Å in ChAc:EG. The shorter H-bond lengths and the increased charged density support the rigidity of the solvate clusters and the measured high viscosities as well as the low conductivities in Ox^{-2}-containing systems. The binding energy for 1:2 ChTFSI:EG (5.45 eV) was lower than those of Ac and Ox^{-2} systems in support of the measured lower viscosities. On the other hand, it was higher than that of 1:2 ChCl:EG (5.36 eV). The Cl system has a higher viscosity (48 cP at 25 °C)[15] than the TFSI-based system and slightly lower viscosity than the Ac system. Previously, we demonstrated that replacing Cl^- with $TFSI^-$ anion can weaken the Coulombic interactions and promote fluidity.[21] Therefore, the lower binding energy for 1:2 ChCl:EG is rather unexpected. This may be because DFT calculations only account for enthalpic contributions to the binding energies without capturing the entropic effects that may be induced by the fluorinated groups in $TFSI^-$. From the measurement of the surface tension and the estimated hole sizes (listed in Table S4), it is seen that ChTFSI:EG has the largest hole size (1.7 Å), consistent with both the decrease in bonding strength between molecules and the low viscosities measured for these mixtures compared to the rest of the systems. Despite the differences in viscosity and bonding strength, the hole size does not change significantly between the 1:4 ChAc:EG (1.51 Å) and Ch_2Ox:EG (1.55 Å), and they are similar to previously reported values for ethaline (1.48 Å).[21] This is because the species that would replace the voids are larger in this system than ethaline; thus they are not as dynamic as ethaline. The 1:2 Ch_2Ox:EG system has the smallest hole size (1.42 Å) in agreement with the increased bonding strength between the salt and EG.

Table 2. Integral Binding Energies Calculated by DFT for the Salt:EG Solvate Clusters

system	composition	integral binding energy (eV)
ChTFSI:EG	1:1	5.06
	1:2	5.45
	1:3	5.92
	1:4	
ChCl:EG	1:1	4.91
	1:2	5.36
	1:3	5.95
	1:4	6.54
ChAc:EG	1:1	5.35
	1:2	5.83
	1:3	6.14
	1:4	6.91
Ch_2Ox:EG	1:1	13.41
	1:2	13.26
	1:3	13.71
	1:4	14.09

The bulk densities of the anion mixtures with EG followed the trend of ChAc < Ch_2Ox < ChTFSI. The increase in density from the Ac^- to Ox^{-2} systems is due to the stronger H-bonding interactions present in the Ch_2Ox:EG system resulting in tighter packing. Densities were highest for the ChTFSI mixtures despite having weaker intermolecular interactions. The large differences in molecular weight between the $TFSI^-$ anion (280.1 g/mol) and the Ox^{-2} (88.0 g/mol) and Ac^- (59.0 g/mol) appear to be significant enough to overcome the differences in bonding strength between the systems.

FTIR spectroscopy was used to study the H-bonding behavior for different compositions of the salts in EG. The spectral region corresponding to the OH stretch of the samples is shown in Figure 3. The full spectra recorded are provided in Figure S3, and the characteristic peaks are listed in Table S5. The specific vibrational modes were identified with the help of the frequencies calculated by DFT (Figures S4–S6 show the calculated and measured IR spectra). The peak at 3300 cm^{-1} seen for EG is associated with ν (OH); the broadness of the peak is due to extensive intermolecular H-bonding between the EG–EG molecules. The addition of the salts disrupts the EG–EG bonding and results in a decrease in peak intensity with increasing salt concentration. Similar changes in FTIR spectra have been observed for mixtures of ChCl and EG.[31] For both ChAc and Ch_2Ox addition, a redshift is seen in the ν (OH) peak, commonly seen for H-bonded molecules[57] (e.g., O–H··· HBA), where the electron density from the HBA transfers to the O–H antibonding orbital causing the bond to weaken and lengthen. The peak shift is more pronounced in the oxalate systems (91 cm^{-1} shift for 1:2 mixture as seen in Figure 3, right) than those with acetate (61 cm^{-1} shift for 1:2 mixture as seen in Figure 3, middle). The larger shift indicates stronger interactions of the Ox^{-2} anion with EG, consistent with the increases in experimental viscosities and the stronger binding energies calculated by DFT. In contrast, ChTFSI addition to EG results in a blueshift (60 cm^{-1} shift for 1:2 molar ratio) due to the weakened H-bonding. The blueshift is caused by O–H bond contraction; this "improper" hydrogen bond is observed in complexes in systems with weaker H-bonding, even in systems dominated by dispersion forces.[57] The blueshift from

https://doi.org/10.1021/acs.jpcc.2c01901
J. Phys. Chem. C XXXX, XXX, XXX–XXX

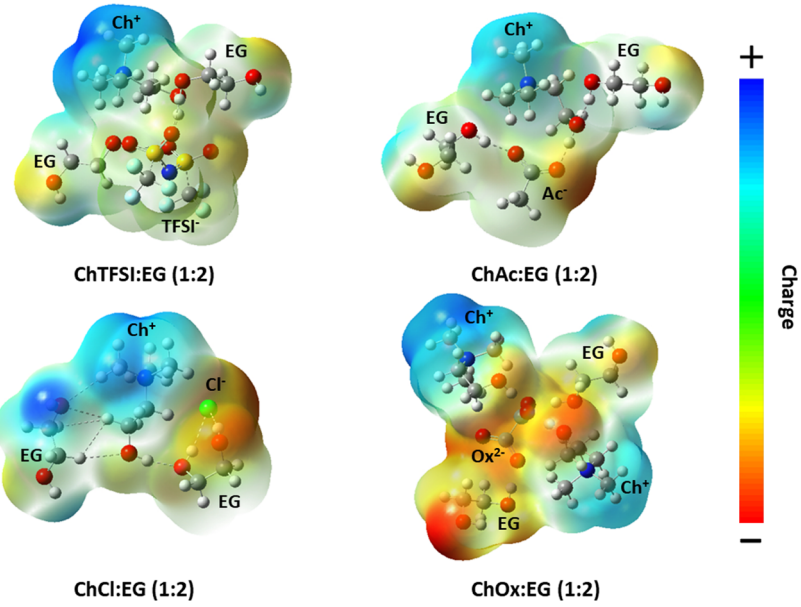

Figure 2. Representative structures of choline salts solvated by two EG molecules. The charge density in terms of the electrostatic potential is shown for all structures with blue representing a relatively positive charge and red representing relative negative charge distribution on a scale of $\pm 7.7 \times 10^{-2}$ V. Atom colors: blue = nitrogen; red = oxygen; green = chloride; yellow = sulfur; gray = carbon; light gray = hydrogen, cyan = fluorine.

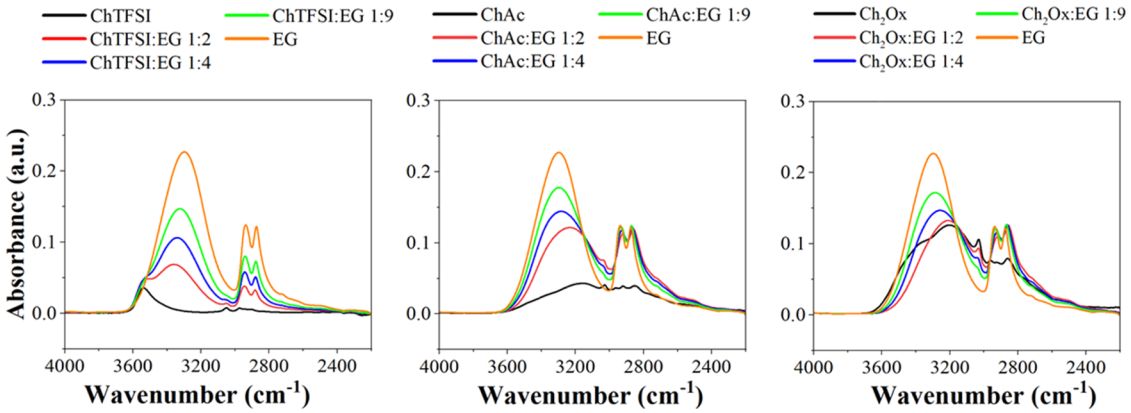

Figure 3. FTIR spectra of ChTFSI:EG (left), ChAc:EG (middle), and Ch_2Ox:EG (right) with 1:2, 1:4, and 1:9 molar compositions. As references, spectra of the Ch salts and EG are included in each panel.

H-bonding arises from the O−H bond shortening caused by TFSI, which is a weaker HBA due to its delocalized charge.

^{1}H NMR was also used to assess changes in H-bonding with composition, specifically focusing on the changes in the hydroxyl protons. NMR spectra of Ch_2Ox:EG systems are shown in Figure 4, while those for ChAc and ChTFSI systems are included in Figures S7−S8. The chemical shift of the hydroxyl proton (denoted "e") on the EG is shifted significantly downfield due to H-bonding with increased Ac^- and Ox^{-2} concentrations. Strong H-bonding interactions deshield the hydroxyl proton by reducing its electron density and lengthening the O−H bond, consistent with what was observed with FTIR. An upfield shift is seen for the hydroxyl proton in the $TFSI^-$ systems as the salt concentration increases. The upfield shift is a result of the $TFSI^-$ anion disrupting the extensive self-H-bonding of the EG; a similar trend was observed in ChCl systems with both Gly and EG as the HBA.[28]

The interfacial densities are probed by the measurement of differential capacitance to gain insights into the general electrode−electrolyte interfacial structure. To determine the electrochemical window to perform the capacitance measurements, CVs were performed (Figure 5, top). Differential capacitance curves of 1:2 mixtures as a function of applied potential are shown in Figure 5 (bottom) for GC (a) and Au (b) working electrodes. Data for the 1:4 molar ratio mixtures are included in Figure S9, exhibiting similar behavior to the 1:2 systems.

In our previous work, we used a modified Gouy−Chapman fit, modeling the interface as a diffuse layer of charge for capacitance data in ChCl-based electrolytes.[12] We discovered that the hydrogen-bonded electrolyte (ChCl:EG) shows similar behavior to the dilute electrolytes on nonmetallic (GC) electrodes. A shallow U-shaped capacitance indicated Ch^+ accumulation upon negative polarization and Cl^- at positive polarization. Capacitance changes at positive potential were weaker due to the Cl^- anion maintaining solvation with EG in the interface much better than the bulky Ch^+ cation. More complex capacitive behavior was observed on metallic electrodes (Au) due to the surface adsorption and formation of

https://doi.org/10.1021/acs.jpcc.2c01901
J. Phys. Chem. C XXXX, XXX, XXX−XXX

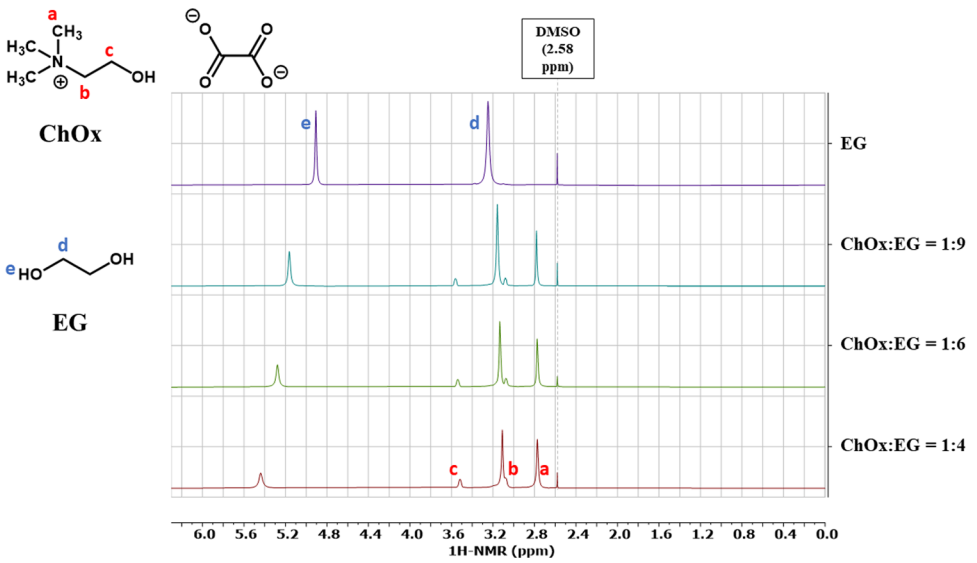

Figure 4. ^{1}H NMR of Ch_2Ox:EG mixtures at 1:4, 1:6, and 1:9 compositions. DMSO peak is the reference at 2.58 ppm. Spectra of EG is included as an additional point of reference.

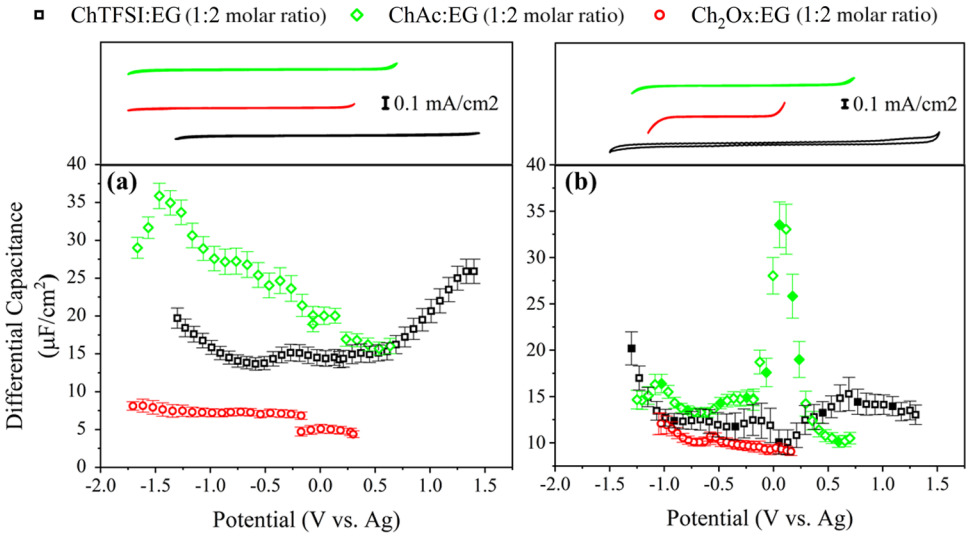

Figure 5. Electrochemical window (top) and differential capacitance curves (bottom) of the 1:2 salt:EG mixtures at GC (a) and Au (b) surfaces. CVs were performed at a scan rate of 20 mV/s. Data points with filled symbols in (b) correspond to potentials used for SERS measurements in Figure 6.

an Au−Cl surface layer. In this work, Ch-based solvents with varied anions in the HBA and analogues to ChCl were used to investigate the capacitive behavior without strongly adsorbed Cl^-. As seen in Figure 5, the ChTFSI systems exhibited a dampened U-shaped differential capacitance on both GC and Au electrodes, similar to the general potential dependence seen for ethaline on a GC surface with minimal differences between −0.5 and 0.0 V.[12] Ch^+ accumulation occurs upon negative polarization in the same way as in ChCl:EG mixtures. The steeper rises in capacitance at positive polarization in $TFSI^-$ systems are due to a decrease in bonding strength between the EG−EG molecules, allowing for more anions to migrate to the electrode interface. The similarity in capacitance between GC and Au surfaces suggests that strong surface adsorption of the anion is less of a dominating factor for ChTFSI:EG solvent on metallic electrodes.

Capacitance was fit using the modified Gouy−Chapman in eq 4 (fit curves are in Figure S10). ChTFSI:EG solvents have interaction parameters, α = (0.020, 0.021) for 1:2 and 1:4 molar ratios, respectively. Compared to ChCl:EG mixtures (α = 0.011, 0.012),[12] TFSI systems had larger α, indicating a decrease in short-range interactions in the solvent due to the bulky $TFSI^-$ anion having delocalized charge density. The weaker bonding due to the $TFSI^-$ anion exhibits behavior more similar to dilute systems. α does not vary significantly between the 1:2 and 1:4 EG mixtures, suggesting that the interaction strength between ions is concentration-independent for these compositions. Debye capacitances for the systems were C_d = (0.96, 0.99 μF), larger than those of Cl systems C_d = (0.60, 0.63 μF),[12] suggesting an increase in the dielectric constant of the interface or a decreasing Debye length.

The ChAc:EG systems exhibit an increase in capacitance at negative potentials on a GC electrode, originating from the Ch^+ accumulation in the interface. A maximum is reached only in the more concentrated 1:2 molar ratio mixture around −1.4 V, which could be due to steric limitations of the Ch^+ at the

https://doi.org/10.1021/acs.jpcc.2c01901
J. Phys. Chem. C XXXX, XXX, XXX−XXX

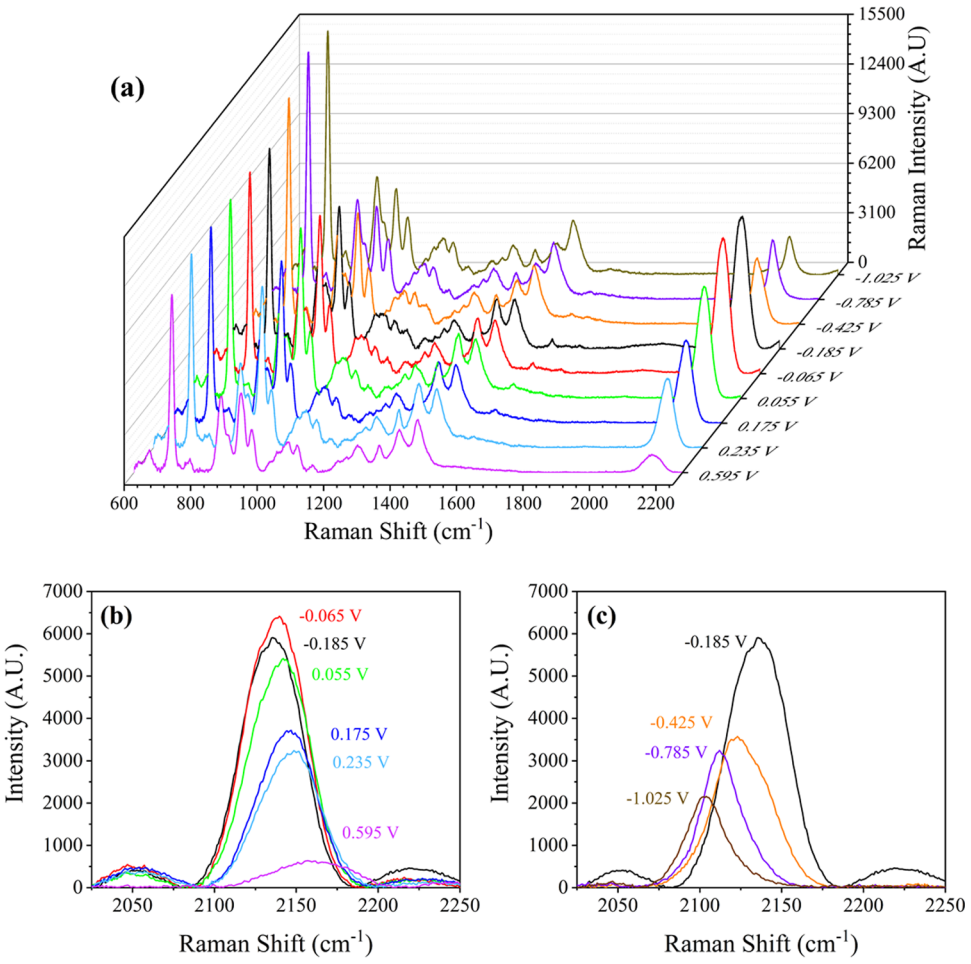

Figure 6. SERS spectra of ChAc:EG (1:2) on an electrochemically roughened Au surface. A wavelength of 785 nm excitation laser and a spectral range of 600−2300 cm^{-1} were used. (a) Raw Raman curves with respect to applied potential. Localized Raman for the region of 2000−2250 cm^{-1}, corresponding to C−O surface interaction at (b) positive and (c) negative polarization, respectively.

surface. No clear increase in capacitance is seen at positive potentials, similar to what we observe on GC for Cl systems, which could be due to the presence of EG at the interface.[12] Surface-adsorbed EG has been confirmed with PM-IRRAS at GC surfaces in DES, particularly at positive potentials.[31] On the Au surface, however, there is not any significant capacity increase upon negative polarization due to Ch^+ accumulation. Instead, a complex capacitive behavior was observed with a maximum at 0.055 V upon positive polarization, suggesting the dominance of anion behavior or some other change in the interface. Similar deviations in capacitive behavior have been observed for ethaline between GC and Au surfaces, which was attributed to the chemisorption of Cl^- and the formation of a surface layer.[12] Interestingly, despite the chemical similarities with the ChAc, the Ch_2Ox system does not present the same behavior. We attribute the difference to the more restricted voltage-induced structuring of Ox^{-2} solvates since they are compact enough to begin with as shown by tighter bond lengths from DFT and increased viscosities. The strong interaction between Ox^{-2} and EG molecules limits mobility and restructuring, whereas it is more likely for Ac^- to desolvate and surface adsorb. The possibility of surface adsorption of Ac^- is further investigated using SERS.

SERS was performed to directly probe the surface layer under polarization. SERS curves for ChAc:EG (1:2) are shown in Figure 6, and normalized curves are included in Figure S11. Potentials of interest were selected based on the differential capacitance curves from EIS (filled symbols in Figure 5b). An example SERS potential sequence for the ChAc:EG 1:2 is included in Figure S12. Table 3 summarizes the vibrational assignments for both the experimental and theoretical Raman spectra in comparison to the literature. Raman modes were calculated using DFT to aid in peak assignment and show relative agreement with experimental modes (see Figure S13). Some deviation is seen between peak placement observed between experiment and theory, which is common and arises from the nature of DFT, as frequencies are calculated for the isolated molecules with no surface to interact with. Ch_2Ox:EG mixtures could not be measured using SERS due to their dark red-brown color, which led to overloading of the signal.

The most significant change in spectral feature is for the peak occurring between 2103 and 2158 cm^{-1}, as seen in Figure 6a. This peak located at 2140 cm^{-1} is only seen in experiments but not in DFT calculations, suggesting that it arises from a surface interaction, possibly of Ac^- forming a COO^-−Au complex, as interpreted in Table 3 or a new species forming at the interface (e.g., gaseous CO) at this potential.[41] Physically dissolved carbon monoxide cannot be present at the beginning of the measurements since the electrolyte was degassed prior to measurements and no electrochemical bias was applied to the electrolyte before its use in EIS and SERS measurements. Additionally, the peak is not observed on the same roughened

https://doi.org/10.1021/acs.jpcc.2c01901
J. Phys. Chem. C XXXX, XXX, XXX−XXX

Table 3. Raman Vibrational Peak Assignments for ChAc:EG and ChTFSI:EG Systems[a]

experimental (cm^{-1})	DFT (cm^{-1})	peak assignments	literature (cm^{-1})
ChAc:EG			
715	701	ν $(N(CH_3))_s$	711,[21] 716[51]
862	862	ν $(CN)_{as}$	877[21]
927	945	ν (C−C) (acetate)	928−926[58,59]
956	963	ρ (CH_3)	956[51]
1060	1057	ν (C−OH)	1065[21]
1094	1085	ν (CH_2)	1092[21]
1273	1262	τ (CH_2)	1295−1305[60]
1340	1360	ν $(CH_3)_{as}$	1344[58]
1398	1410	ν (CO)	1400,[61] 1413[58]
1454	1457	ω (CH_2)	1442[21]
		ω (CH_3)	1445[51]
2103−2158		COO^--Au	
ChTFSI:EG			
710	729	ν $(N(CH_3))_s$	711,[21] 716[51]
737	742	breathing mode	739,[21] 743[62]
864	863	ν $(CN)_{as}$	877[21]
951	942	ρ (CH_3)	956[51]
1133	1118	ν $(SO_2)_s$	1133[21]
		ν $(N-S)_{as}$	1136[62]
1239	1208	ν $(CF)_s$	1241[21]
			1242[62]
1451	1419	ω (CH_2)	1463[21]
		ω (CH_3)	

[a]Abbreviations: ν, stretch; ω, wagging; τ, twisting; ρ, rocking; s, symmetric; as, antisymmetric.

Au surfaces in other systems, ruling out the peak being residual from the processing of the surface. Since the peak we observe is present before any polarization is applied, it is unlikely to be a result of carbon monoxide from electrolyte degradation. This is further probed by electrolysis experiments as discussed later.

The intensity of the peak at 2140 cm^{-1} is strongest between −0.425 and 0.235 V, consistent with the potential region where complex capacitive behavior is observed in Figure 5b. While prior SERS literature with aqueous electrolytes reports vibrations at 1400 cm^{-1} for the acetate at lower concentrations,[61] and none around 2140 cm^{-1}, we observe close correlations of this additional peak with other Ac^- vibrations. Specifically, 923 cm^{-1} (ν (C−C)) and 1397 cm^{-1} (ν (CO)) decrease with stronger polarization, following a similar trend to the 2140 cm^{-1} peak (Figure S14). Therefore, our interpretation is that this is more likely due to the specific surface interaction of Ac- through its $-COO^-$ functionality. Stark shifts are seen in Figure S15 for the COO^--Au peak with applied potential with a shift rate of 32 cm^{-1}/V, indicating interactions of the Ac^- with the electrode surface. The measured shift rate is higher than the typical range of 5−20 cm^{-1}/V due to the strong Ac^-−EG interactions through H-bonding.[63] As seen in Figure 6b, there is a blueshift from 2135 to 2158 cm^{-1} for COO^-−Au with increased positive polarization, which indicates increased interactions for the Au surface and the Ac^- anion. The redshift from 2135 to 2103 cm^{-1} in Figure 6c upon negative polarization, accompanied by reduced intensity is indicative of the lengthening of the Au−Ac^- bonds.

A general decrease in Ac^- peak intensities is seen as the potential was swept from OCP to more negative potentials as a result of the Ac^- getting replaced by the Ch^+ cation. Figure S14 shows intensity changes with potential for the vibrational modes of the Ch^+ and the Ac^-. On the other hand, as the potential was swept in the positive direction, the Ac^- peak intensities also decrease, resulting in maximum intensity around OCP. The governing mechanism for this phenomenon is not clear from these experiments alone; however, a possible explanation is the reorientation of the Ac^- and different coordination to the surface such as the switch between binding to the surface through both oxygens to a single oxygen.

Other spectral changes were the increases in intensities for the peaks of 715, 862, and 1094 cm^{-1} corresponding to the ν $(N(CH_3))_s$, ν $(CN)_{as}$, and ν (Ch_2) of the cation, upon increasingly negative potentials applied from OCP. This trend was more prominent between −0.425 and −1.025 V. This further supports the discussion of the excess Ac^- on the surface being displaced with Ch^+ upon negative polarization. The combined SERS and EIS results indicate that surface adsorption is playing a dominant role in charge density at the interface in the ChAc system. This is likely true for other organic-based anions.

To eliminate the possibility of CO formation upon applied potentials in EIS and SERS, additional CPE experiments were performed. Figure S16 shows chronoamperometric plots of the deaerated ChAc:EG at 0.055 V, 0.7 V, −1.25 V (vs Ag), and −2.5 V (vs Ag), where no electrolyte degradation was detected, except at −2.5 V, which is beyond the stability window as seen in the CV in Figure 5. The same can be confirmed from TCD and FID response of GC where no gaseous products were detected at 0.055, 0.7, and −1.25 V (Figure S17). The ^1H and ^{13}C NMR spectra of ChAc:EG before and after 40 min electrolysis at 0.055, 0.7, and −1.25 V (vs Ag) also show no change and no measurable degradation products in the liquid phase (Figures S18−S19). On the other hand, the CPE experiments at −2.5 V (vs Ag) showed electrolyte breakdown with current density exceeding 8 mA/cm^2. This was accompanied by methane and ethane formation as detected by online GC (Figure S17), from the electrochemical oxidation of Ac^- at very high negative potentials.[64] These results suggest that the peak seen in SERS at 2140 cm^{-1} is unlikely to be due to CO.

In comparison to the acetate system, characteristic peaks for the 1:2 ChTFSI:EG 1:2 tabulated in Table 3 show little change in peak intensity and location under polarization. Raw and normalized curves for 1:2 ChTFSI:EG can be found in Figures S20−S21. Raman frequencies calculated by theory show relatively good agreement with experimental modes as seen in Figure S22. Unlike the ChAc systems, there was no evidence of potential-dependent surface adsorption in the ChTFSI:EG system in SERS spectra. This is consistent with the similarity observed between differential capacitance on GC and Au surfaces, suggesting surface adsorption is not dominant. Anion choice is very important when developing H-bonded electrolytes as surface-adsorbed species can drastically impact kinetics in electrochemical applications.

CONCLUSIONS

A fundamental understanding of interface structure and the bulk properties of DESs and similar concentrated hydrogen-bonded electrolytes is essential for their applications in electrochemical processes. In this work, how the anion of the choline salt impacts the bulk properties and interfacial structure of H-bonded electrolytes is shown. The charge

https://doi.org/10.1021/acs.jpcc.2c01901
J. Phys. Chem. C XXXX, XXX, XXX−XXX

density on the ions was found to significantly impact the strength of H-bonding and ion interactions in these mixtures. Calculated energetics of anion solvation and complexation using DFT showed the strength of bonding in the anion systems follows the trend ChTFSI < ChAc < Ch_2Ox. Systems with increased binding energies exhibited increases in viscosity and decreases in conductivity.

It was found that surface adsorption is still present in systems with organic anions, playing a dominant role in interfacial behavior. The complex capacitive behavior for ChAc:EG systems on Au surfaces was determined to be due to the adsorption of the acetate anion and was confirmed with SERS. The observed Ac^- adsorption is similar to adsorption of the COO^- group of the small-molecule additive nicotinic acid used to displace Cl^- in ethaline to achieve mirror quality deposits of Zn.[2] The need for additives to yield smooth uniform deposits can be eliminated by Cl-free DESs. Further studies investigating electrodeposition in the ChAc:EG systems could be valuable for realizing smooth coatings.

In systems where anion adsorption is not dominant, a broad U-shaped capacitance was measured for the H-bonded concentrated electrolyte that seems to be behaving similar to dilute systems. It was also found that the strong bonding interactions in the Ch_2Ox:EG inhibit changes in interfacial charge density and prevent surface adsorption of Ox^{-2}. The anion size, ion charge density, and interaction strength in concentrated H-bonded electrolytes influence ion packing, dynamics, and interfacial behavior. This understanding is necessary for advancing electrolytes to improve kinetics and electrodeposit morphology in electrochemical processes.

■ ASSOCIATED CONTENT

Supporting Information

The Supporting Information is available free of charge at https://pubs.acs.org/doi/10.1021/acs.jpcc.2c01901.

NMR and FTIR spectra of the synthesized samples; tabulated densities, surface tension, viscosity, and conductivity along with fitting parameters; DFT differential binding energies; differential capacitance curves for the 1:4 mixtures; modified Gouy−Chapman fits; additional SERS analysis; and electrochemical degradation analysis (PDF)

■ AUTHOR INFORMATION

Corresponding Author

Burcu Gurkan − *Chemical and Biomolecular Engineering, Case Western Reserve University, Cleveland, Ohio 44106, United States;* orcid.org/0000-0003-4886-3350; Email: beg23@case.edu

Authors

William Dean − *Chemical and Biomolecular Engineering, Case Western Reserve University, Cleveland, Ohio 44106, United States*

Drace Penley − *Chemical and Biomolecular Engineering, Case Western Reserve University, Cleveland, Ohio 44106, United States*

Yun-Yang Lee − *Chemical and Biomolecular Engineering, Case Western Reserve University, Cleveland, Ohio 44106, United States;* orcid.org/0000-0002-4165-0857

Raziyeh Ghahremani − *Chemical and Biomolecular Engineering, Case Western Reserve University, Cleveland, Ohio 44106, United States*

Saudagar Dongare − *Chemical and Biomolecular Engineering, Case Western Reserve University, Cleveland, Ohio 44106, United States*

Complete contact information is available at: https://pubs.acs.org/10.1021/acs.jpcc.2c01901

Author Contributions

W.D. performed experiments and analyzed results for physical property, electrochemical, and spectroscopic measurements. D.P. performed DFT calculations to determine binding energies and vibrational Raman frequencies. Y.-Y.L. assisted in synthesis and performed NMR measurements. R.G. assisted in the experimental analysis of physical properties. S.D. performed the degradation experiments and analysis. B.G. contributed to the design of experimental plans and discussion of the results. The manuscript was written through contributions of all authors. All authors have approved the final version of this manuscript.

Notes

The authors declare no competing financial interest.

■ ACKNOWLEDGMENTS

This project was supported by the Breakthrough Electrolytes for Energy Storage (BEES), an Energy Frontier Center of the U.S. Department of Energy. Award No. DE-SC0019409. Theoretical calculations were performed using the High-Performance Computing Resource in the Core Facility for Advanced Research Computing at Case Western Reserve University. D.P. was supported by the National Science Foundation, Chemical, Bioengineering, Environmental and Transport Systems under award number 1903259. The authors thank Case Applied Raman Laboratory for access to the Horiba 785 nm instrument.

■ REFERENCES

(1) Endres, F.; Abbott, A.; MacFarlane, D. R. *Electrodeposition from Ionic Liquids*; Wiley-VCH: Weinheim, 2008.

(2) Alesary, H. F.; Cihangir, S.; Ballantyne, A. D.; Harris, R. C.; Weston, D. P.; Abbott, A. P.; Ryder, K. S. Influence of Additives on the Electrodeposition of Zinc from a Deep Eutectic Solvent. *Electrochim. Acta* **2019**, *304*, 118−130.

(3) Abbott, A. P.; El Ttaib, K.; Frisch, G.; McKenzie, K. J.; Ryder, K. S. Electrodeposition of Copper Composites from Deep Eutectic Solvents Based on Choline Chloride. *Phys. Chem. Chem. Phys.* **2009**, *11*, 4269−4277.

(4) Zhang, L.; Zhang, C.; Ding, Y.; Ramirez-Meyers, K.; Yu, G. A Low-Cost and High-Energy Hybrid Iron-Aluminum Liquid Battery Achieved by Deep Eutectic Solvents. *Joule* **2017**, *1*, 623−633.

(5) Yamagata, M.; Tachikawa, N.; Katayama, Y.; Miura, T. Electrochemical Behavior of Several Iron Complexes in Hydrophobic Room-Temperature Ionic Liquids. *Electrochim. Acta* **2007**, *52*, 3317−3322.

(6) Schaltin, S.; Li, Y.; Brooks, N. R.; Sniekers, J.; Vankelecom, I. F. J.; Binnemans, K.; Fransaer, J. Towards an All-Copper Redox Flow Battery Based on a Copper-Containing Ionic Liquid. *Chem. Commun.* **2016**, *52*, 414−417.

(7) Lloyd, D.; Vainikka, T.; Ronkainen, M.; Kontturi, K. Characterisation and Application of the Fe(II)/Fe(III) Redox Reaction in an Ionic Liquid Analogue. *Electrochim. Acta* **2013**, *109*, 843−851.

(8) Xu, Q.; Qin, L. Y.; Ji, Y. N.; Leung, P. K.; Su, H. N.; Qiao, F.; Yang, W. W.; Shah, A. A.; Li, H. M. A Deep Eutectic Solvent (DES)

Electrolyte-Based Vanadium-Iron Redox Flow Battery Enabling Higher Specific Capacity and Improved Thermal Stability. *Electrochim. Acta* **2019**, *293*, 426−431.
(9) Zhang, C.; Qian, Y.; Ding, Y.; Zhang, L.; Guo, X.; Zhao, Y.; Yu, G. Biredox Eutectic Electrolytes Derived from Organic Redox-Active Molecules: High-Energy Storage Systems. *Angew. Chem., Int. Ed.* **2019**, *58*, 7045−7050.
(10) Hansen, B. B.; Spittle, S.; Chen, B.; Poe, D.; Zhang, Y.; Klein, J. M.; Horton, A.; Adhikari, L.; Zelovich, T.; Doherty, B. W.; et al. Deep Eutectic Solvents: A Review of Fundamentals and Applications. *Chem. Rev.* **2021**, *121*, 1232−1285.
(11) Abbott, A. P.; Boothby, D.; Capper, G.; Davies, D. L.; Rasheed, R. K. Deep Eutectic Solvents Formed between Choline Chloride and Carboxylic Acids: Versatile Alternatives to Ionic Liquids. *J. Am. Chem. Soc.* **2004**, *126*, 9142−9147.
(12) Dean, W.; Klein, J.; Gurkan, B. Do Deep Eutectic Solvents Behave Like Ionic Liquid Electrolytes? A Perspective from the Electrode-Electrolyte Interface. *J. Electrochem. Soc.* **2021**, *168*, 026503.
(13) Hammond, O. S.; Bowron, D. T.; Edler, K. J. Liquid Structure of the Choline Chloride-Urea Deep Eutectic Solvent (Reline) from Neutron Diffraction and Atomistic Modelling. *Green Chem.* **2016**, *18*, 2736−2744.
(14) Zhang, Y.; Poe, D.; Heroux, L.; Squire, H.; Doherty, B. W.; Long, Z.; Dadmun, M.; Gurkan, B.; Tuckerman, M. E.; Maginn, E. J. Liquid Structure and Transport Properties of the Deep Eutectic Solvent Ethaline. *J. Phys. Chem. B* **2020**, *124*, 5251−5264.
(15) Alfurayj, I.; Fraenza, C. C.; Zhang, Y.; Pandian, R.; Spittle, S.; Hansen, B.; Dean, W.; Gurkan, B.; Savinell, R.; Greenbaum.; et al. Solvation Dynamics of Wet Ethaline: Water Is the Magic Component. *J. Phys. Chem. B* **2021**, *125*, 8888−8901.
(16) Shaheen, N. A.; Ijjada, M.; Vukmirovic, M. B.; Akolkar, R. Mechanism of Electrochemical Oxidation of Nitroxide Radicals in Ethaline Deep Eutectic Solvent. *J. Electrochem. Soc.* **2020**, *167*, 143505.
(17) Abbott, A. P.; Barron, J. C.; Ryder, K. S.; Wilson, D. Eutectic-Based Ionic Liquids with Metal-Containing Anions and Cations. *Chem. − Eur. J.* **2007**, *13*, 6495−6501.
(18) Ibrahim, R. K.; Hayyan, M.; AlSaadi, M. A.; Ibrahim, S.; Hayyan, A.; Hashim, M. A. Physical Properties of Ethylene Glycol-Based Deep Eutectic Solvents. *J. Mol. Liq.* **2019**, *276*, 794−800.
(19) Guo, W.; Hou, Y.; Ren, S.; Tian, S.; Wu, W. Formation of Deep Eutectic Solvents by Phenols and Choline Chloride and Their Physical Properties. *J. Chem. Eng. Data* **2013**, *58*, 866−872.
(20) Abbott, A. P.; Harris, R. C.; Ryder, K. S.; D'Agostino, C.; Gladden, L. F.; Mantle, M. D. Glycerol Eutectics as Sustainable Solvent Systems. *Green Chem.* **2011**, *13*, 82−90.
(21) Klein, J. M.; Squire, H.; Dean, W.; Gurkan, B. E. From Salt in Solution to Solely Ions: Solvation of Methyl Viologen in Deep Eutectic Solvents and Ionic Liquids. *J. Phys. Chem. B* **2020**, *124*, 6348−6357.
(22) Du, C.; Zhao, B.; Chen, X.-B.; Birbilis, N.; Yang, H. Effect of Water Presence on Choline Chloride−2urea Ionic Liquid and Coating Platings from the Hydrated Ionic Liquid. *Sci. Rep.* **2016**, *6*, No. 29225.
(23) Shah, D.; Mjalli, F. S. Effect of Water on the Thermo-Physical Properties of Reline: An Experimental and Molecular Simulation Based Approach. *Phys. Chem. Chem. Phys.* **2014**, *16*, 23900−23907.
(24) Gurkan, B.; Squire, H.; Pentzer, E. Metal-Free Deep Eutectic Solvents: Preparation, Physical Properties, and Significance. *J. Phys. Chem. Lett.* **2019**, *10*, 7956−7964.
(25) Zhang, Q.; De Oliveira Vigier, K.; Royer, S.; Jérôme, F. Deep Eutectic Solvents: Syntheses, Properties and Applications. *Chem. Soc. Rev.* **2012**, *41*, 7108−7146.
(26) Shen, D.; Steinberg, K.; Akolkar, R. Avoiding Pitfalls in the Determination of Reliable Electrochemical Kinetics Parameters for the Cu2+ → Cu1+ Reduction Reaction in Deep Eutectic Solvents. *J. Electrochem. Soc.* **2018**, *165*, E808−E815.
(27) Zhen, F.; Percevault, L.; Paquin, L.; Limanton, E.; Lagrost, C.; Hapiot, P. Electron Transfer Kinetics in a Deep Eutectic Solvent. *J. Phys. Chem. B* **2020**, *124*, 1025−1032.
(28) Spittle, S.; Poe, D.; Doherty, B.; Kolodziej, C.; Heroux, L.; Haque, M. A.; Squire, H.; Cosby, T.; Zhang, Y.; Fraenza, C.; et al. Evolution of Microscopic Heterogeneity and Dynamics in Choline Chloride-Based Deep Eutectic Solvents. *Nat. Commun.* **2022**, *13*, No. 1081.
(29) Shen, D.; Vukmirovic, M. B.; Akolkar, R. Understanding the Role of Complexation in the Charge-Transfer Kinetics of the Cu 2+ + e ↔ Cu 1+ Redox Reaction in Ethaline Deep Eutectic Solvent. *J. Electrochem. Soc.* **2019**, *166*, E526−E532.
(30) Shen, X.; Sinclair, N.; Wainright, J.; Akolkar, R.; Savinell, R. F. Evaluating and Developing a Reliable Reference Electrode for Choline Chloride Based Deep Eutectic Solvents. *J. Electrochem. Soc.* **2020**, *167*, 086509.
(31) Vieira, L.; Schennach, R.; Gollas, B. In Situ PM-IRRAS of a Glassy Carbon Electrode/Deep Eutectic Solvent Interface. *Phys. Chem. Chem. Phys.* **2015**, *17*, 12870−12880.
(32) Chen, Z.; McLean, B.; Ludwig, M.; Stefanovic, R.; Warr, G. G.; Webber, G. B.; Page, A. J.; Atkin, R. Nanostructure of Deep Eutectic Solvents at Graphite Electrode Interfaces as a Function of Potential. *J. Phys. Chem. C* **2016**, *120*, 2225−2233.
(33) Figueiredo, M.; Gomes, C.; Costa, R.; Martins, A.; Pereira, C. M.; Silva, F. Differential Capacity of a Deep Eutectic Solvent Based on Choline Chloride and Glycerol on Solid Electrodes. *Electrochim. Acta* **2009**, *54*, 2630−2634.
(34) Gouy, M. Sur La Constitution de La Charge Électrique à La Surface d'un Électrolyte. *J. Phys. Theor. Appl.* **1910**, *9*, 457−468.
(35) Chapman, D. L. LI. A Contribution to the Theory of Electrocapillarity. *Lond. Edinb. Dublin Philos. Mag. J. Sci.* **1913**, *25*, 475−481.
(36) Wu, J.; Zhou, R.; Radjenovic, P. M.; Liu, S.; Wu, D.; Li, J.; Mao, B.; Yan, J. Electrochemical Impedance Spectroscopy and Raman Spectroscopy Studies on Electrochemical Interface between Au(111) Electrode and Ethaline Deep Eutectic Solvent. *Electrochim. Acta* **2021**, *390*, 138859.
(37) Wu, J.; Liu, S.; Tan, Z.; Guo, Y.; Zhou, J.; Mao, B.; Yan, J. Effect of Hydrogen Bond Donor Molecules Ethylene Glycerol and Lactic Acid on Electrochemical Interfaces in Choline Chloride Based-Deep Eutectic Solvents. *J. Chem. Phys.* **2021**, *155*, 244702.
(38) Atilhan, M.; Aparicio, S. Deep Eutectic Solvents on the Surface of Face Centered Cubic Metals. *J. Phys. Chem. C* **2016**, *120*, 10400−10409.
(39) Mamme, M. H.; Moors, S. L. C.; Terryn, H.; Deconinck, J.; Ustarroz, J.; De Proft, F. Atomistic Insight into the Electrochemical Double Layer of Choline Chloride-Urea Deep Eutectic Solvents: Clustered Interfacial Structuring. *J. Phys. Chem. Lett.* **2018**, *9*, 6296−6304.
(40) Abbott, A. P.; Barron, J. C.; Frisch, G.; Ryder, K. S.; Silva, A. F. The Effect of Additives on Zinc Electrodeposition from Deep Eutectic Solvents. *Electrochim. Acta* **2011**, *56*, 5272−5279.
(41) Li, J. F.; Huang, Y. F.; Ding, Y.; Yang, Z. L.; Li, S. B.; Zhou, X. S.; Fan, F. R.; Zhang, W.; Zhou, Z. Y.; Wu, D. Y.; et al. Shell-Isolated Nanoparticle-Enhanced Raman Spectroscopy. *Nature* **2010**, *464*, 392−395.
(42) Wang, Y.-H.; Liang, M.; Zhang, Y.; Chen, S.; Radjenovic, P.; Zhang, H.; Yang, Z.; Zhou, X.; Tian, Z.; Li, J. Probing Interfacial Electronic and Catalytic Properties on Well-Defined Surfaces by Using In Situ Raman Spectroscopy. *Angew. Chem., Int. Ed.* **2018**, *57*, 11257−11261.
(43) Jeanmaire, D. L.; Van Duyne, R. P. Surface Raman Spectroelectrochemistry: Part I. Heterocyclic, Aromatic, and Aliphatic Amines Adsorbed on the Anodized Silver Electrode. *J. Electroanal. Chem. Interfacial Electrochem.* **1977**, *84*, 1−20.
(44) Li, J.-F.; Ding, S.; Yang, Z.; Bai, M.; Anema, J. R.; Wang, X.; Wang, A.; Wu, D.; Ren, B.; Hou, S.; Wandlowski, T.; Tian, Z. Q. Extraordinary Enhancement of Raman Scattering from Pyridine on

https://doi.org/10.1021/acs.jpcc.2c01901
J. Phys. Chem. C XXXX, XXX, XXX−XXX

Single Crystal Au and Pt Electrodes by Shell-Isolated Au Nanoparticles. *J. Am. Chem. Soc.* **2011**, *133*, 15922−15925.
(45) Klein, J. M.; Squire, H.; Gurkan, B. Electroanalytical Investigation of the Electrode-Electrolyte Interface of Quaternary Ammonium Ionic Liquids: Impact of Alkyl Chain Length and Ether Functionality. *J. Phys. Chem. C* **2020**, *124*, 5613−5623.
(46) Bockris, J. O.; Reddy, A. K. N. *Modern Electrochemistry*; Bockris, J. O., Ed.; Springer, 1998; Vol. *1*, DOI: DOI: 10.1007/b114546.
(47) Frisch, M. J.; Trucks, G. W.; Schlegel, H. B.; Scuseria, G. E.; Robb, M.; Cheeseman, J. R.; Scalmani, G.; Barone, V.; Petersson, G.; Nakatsuji, H.et al. *Wallin-Gaussian 16*, Revision C.01; Gaussian, Inc.: Wallin, 2016.
(48) Lee, C.; Yang, W.; Parr, R. G. Development of the Colle-Salvetti Correlation-Energy Formula into a Functional of the Electron Density. *Phys. Rev. B* **1988**, *37*, 785−789.
(49) Ditchfield, R.; Hehre, W. J.; Pople, J. A. Self-Consistent Molecular-Orbital Methods. IX. An Extended Gaussian-Type Basis for Molecular-Orbital Studies of Organic Molecules. *J. Chem. Phys.* **1971**, *54*, 724−728.
(50) Palafox, M. A. DFT Computations on Vibrational Spectra: Scaling Procedures to Improve the Wavenumbers *Phys. Sci. Rev.* 2018, *36* DOI: 10.1515/psr-2017-0184.
(51) de Souza, Í. F. T.; Ribeiro, M. C. C. A Raman Spectroscopy and Rheology Study of the Phase Transitions of the Ionic Liquid Choline Acetate. *J. Mol. Liq.* **2021**, *322*, 114530.
(52) Penley, D.; Vicchio, S. P.; Getman, R. B.; Gurkan, B. Energetics of Li+ Coordination with Asymmetric Anions in Ionic Liquids by Density Functional Theory. *Front. Energy Res.* **2021**, *9*, 570.
(53) Klein, J. M.; Panichi, E.; Gurkan, B. Potential Dependent Capacitance of [EMIM][TFSI], [N 1114][TFSI] and [PYR 13][TFSI] Ionic Liquids on Glassy Carbon. *Phys. Chem. Chem. Phys.* **2019**, *21*, 3712−3720.
(54) Lockett, V.; Sedev, R.; Ralston, J.; Horne, M.; Rodopoulos, T. Differential Capacitance of the Electrical Double Layer in Imidazolium-Based Ionic Liquids: Influence of Potential, Cation Size, and Temperature. *J. Phys. Chem. C* **2008**, *112*, 7486−7495.
(55) Wang, W.; Huang, Y.; Liu, D.; Wang, F.; Tian, Z.; Zhan, D. Electrochemically Roughened Gold Microelectrode for Surface-Enhanced Raman Spectroscopy. *J. Electroanal. Chem.* **2016**, *779*, 126−130.
(56) Gao, P.; Gosztola, D.; Leung, L.-W. H.; Weaver, M. J. Surface-Enhanced Raman Scattering at Gold Electrodes: Dependence on Electrochemical Pretreatment Conditions and Comparisons with Silver. *J. Electroanal. Chem. Interfacial Electrochem.* **1987**, *233*, 211−222.
(57) Joseph, J.; Jemmis, E. D. Red-, Blue-, or No-Shift in Hydrogen Bonds: A Unified Explanation. *J. Am. Chem. Soc.* **2007**, *129*, 4620−4632.
(58) Ito, K.; Bernstein, H. J. The Vibrational Spectra of the Formate, Acetate, and Oxalate Ions. *Can. J. Chem.* **1956**, *34*, 170−178.
(59) Gültekin, D.; Akbulut, H. *Raman Studies of ZnO Products Synthesized by Solution Based Methods*; Polish Academy of Sciences, 2016; Vol. *129*, pp 803−805. DOI: DOI: 10.12693/APhysPolA.129.803.
(60) In-Vien, D.; Colthup, N. B.; Fateley, W. G.; Grasselli, J. G. B. T. *The Handbook of Infrared and Raman Characteristic Frequencies of Organic Molecules*; Academic Press: San Diego, 1991; p iii. DOI: DOI: 10.1016/B978-0-08-057116-4.50001-8.
(61) Delgado, J. M.; Orts, J. M.; Pérez, J. M.; Rodes, A. Sputtered Thin-Film Gold Electrodes for in Situ ATR-SEIRAS and SERS Studies. *J. Electroanal. Chem.* **2008**, *617*, 130−140.
(62) Liu, T. Electrodéposition de Couches Minces Métalliques à Partir de Solutions de Liquides Ioniques Pour Des Applications Électroniques. *L'archive ouverte pluridisciplinaire HAL* **2015**, HAL Id: tel-01142699.
(63) Bhattacharyya, D.; Videla, P. E.; Cattaneo, M.; Batista, V. S.; Lian, T.; Kubiak, C. P. Vibrational Stark Shift Spectroscopy of Catalysts under the Influence of Electric Fields at Electrode−Solution Interfaces. *Chem. Sci.* **2021**, *12*, 10131−10149.
(64) Peng, X.; Omasta, T.; Zhao, X.; Mustain, W. E. Electrochemical Pathways for Electrochemical Oxidation of Acetic Acid. *ECS Trans.* **2018**, *85*, 29−34.

https://doi.org/10.1021/acs.jpcc.2c01901
J. Phys. Chem. C XXXX, XXX, XXX−XXX